

1 **Impact of convective organization on the response of tropical**
2 **precipitation extremes to warming**

3 CAROLINE MULLER *

Atmospheric and Oceanic Sciences Program, Princeton University, Princeton, New Jersey

* *Corresponding author address:* Caroline Muller, Princeton University/GFDL, 300 Forrestal Road,
Princeton, NJ 08540.

E-mail: carolinemuller123@gmail.com

ABSTRACT

5 This study examines the response of tropical precipitation extremes to warming in organized
6 convection using a cloud-resolving model. Vertical shear is imposed to organize the convec-
7 tion into squall lines. Earlier studies show that in disorganized convection, the fractional
8 increase of precipitation extremes is similar to that of surface water vapor, which is substan-
9 tially smaller than the increase in column water vapor. It has been suggested that organized
10 convection could lead to stronger amplifications.

11 But regardless of the strength of the shear, amplifications of precipitation extremes in
12 the cloud-resolving simulations are comparable to those of surface water vapor, and are
13 substantially less than increases in column water vapor. The results without shear and
14 with critical shear, for which the squall lines are perpendicular to the shear, are surprisingly
15 similar with a fractional rate of increase of precipitation extremes slightly smaller than that of
16 surface water vapor. Interestingly, the dependence on shear is non-monotonic, and stronger
17 supercritical shear yields larger rates, close to or slightly larger than surface humidity.

18 A scaling is used to evaluate the thermodynamic and dynamic contributions to precipita-
19 tion extremes changes. To first order, they are dominated by the thermodynamic component
20 which has the same magnitude for all shears, close to the change in surface water vapor. The
21 dynamic contribution plays a secondary role, and tends to weaken extremes without shear
22 and with critical shear, while it strenghtens extremes with supercritical shear. These dif-
23 ferent dynamic contributions for different shears are due to different responses of convective
24 mass fluxes in individual updrafts to warming.

1. Introduction

The response of the hydrological cycle to climate change has many societal impacts. Both changes in mean precipitation and in precipitation extremes are expected with an increase in surface temperatures. It is well known that the change in global mean precipitation is constrained by energetics (Allen and Ingram 2002; Held and Soden 2006; Muller and O’Gorman 2011). Specifically, the changes in latent heat from precipitation and in surface sensible heat flux have to balance the change in atmospheric radiative cooling (1). This energetic constraint limits the increase of global mean precipitation to a rate of about 2 % K^{-1} in simulations of twenty-first century climate change (Held and Soden 2006), much lower than the increase in the availability of moisture in a warmer climate, from 6 % to 12 % K^{-1} depending on latitude (O’Gorman and Muller 2010). Given the small changes in model relative humidity (Soden and Held 2006), the atmospheric humidity is expected to increase according to the Clausius-Clapeyron (CC) equation, which predicts an approximately exponential increase with temperature. An increase in atmospheric humidity has already been observed in recent years (Trenberth 2011). Over oceans, the increases are consistent with CC expectations with a constant relative humidity, while increases are somewhat lower over land especially where water availability is limited.

Changes in regional precipitation or in precipitation extremes on the other hand, need not be constrained by global mean energetics. For the former, Muller and O’Gorman (2011) find that in simulations of twenty-first century climate change, changes in radiative and surface sensible heat fluxes are a guide to the regional precipitation response over land and at large scales (thousands of kilometers), but not at small scales over the ocean. For precipitation extremes, it has been argued that the heaviest rainfall events occur when effectively all the moisture in a volume of air is precipitated out (Trenberth 1999; Allen and Ingram 2002; Pall et al. 2007). This implies that the rate of increase of precipitation extremes should follow the increase in atmospheric humidity, and could be even larger if vertical mass fluxes in convective updrafts were to increase. In the mean, the upward mass flux from tropical

convection decreases with increasing temperatures (Betts 1998; Held and Soden 2006; Vecchi and Soden 2007), but the response in the individual convective towers leading to the heaviest rainfall rates could be different.

In observations of present-day variability, precipitation extremes have been found to increase at a greater fractional rate than the amount of atmospheric water vapor (Allan and Soden 2008; Lenderink and van Meijgaard 2008; Liu et al. 2009; Lenderink et al. 2011). Although present-day variability may not be directly relevant to global warming, this raises the possibility that tropical precipitation extremes could increase faster than CC expectations. Results from climate change simulations in general circulation models (GCMs) give widely divergent changes in precipitation extremes in the tropics (Emori and Brown 2005; O’Gorman and Schneider 2009; Sugiyama et al. 2010). For example, O’Gorman and Schneider (2009) find that the rate of increase of tropical precipitation extremes in the third Coupled Model Intercomparison Project (CMIP3) climate model simulations ranged from 1.3% to 30% depending on the climate model. The inability of current climate models to consistently predict changes in tropical precipitation extremes with warming is likely tied to the use of convective parameterizations (Wilcox and Donner 2007), and is not surprising given the failure of the climate models to simulate observed tropical precipitation extremes in the present climate (Kharin et al. 2007).

This motivates the use of high-resolution cloud-resolving models (CRMs) to address this issue. Because of their large computational costs, such models are typically run in idealized settings (e.g. on square, doubly-periodic domains over ocean with simplified microphysics), but they have the advantage that they resolve the convective-scale processes instead of parameterizing them. Recently, Romps (2011) and Muller et al. (2011) (hereafter MOB11) used CRMs to investigate the response of precipitation extremes to warming in radiative-convective equilibrium over ocean in the absence of convective organization. Despite some important differences in the settings (different CRMs, small versus large domain, fine versus coarse resolution, different Sea Surface Temperature (SST) increases, interactive versus fixed

radiative cooling rates), their conclusions are the same: the amplification of precipitation extremes with warming follows the increase in cloud-base water vapor, or surface Clausius-Clapeyron scaling (CC_{sfc}), which is smaller than the increase in vertically-integrated atmospheric humidity, or Clausius-Clapeyron scaling (CC). In the tropics, using column water vapor as a proxy for the rate of change of precipitation extremes instead of surface humidity can lead to substantial overestimates. O’Gorman and Muller (2010) find that for climate model simulations of the A1B emissions scenario, the multimodel mean rate of increase in zonal mean column water vapor is 8.4% at the equator, whereas the increase in surface specific humidity is only 5.8%, yielding an overestimate of about 45%. Both CRM studies find that the increased SSTs yield an upward shift of atmospheric variables, consistent with the upward shift of the temperature profile on a warmer moist adiabat (Singh and O’Gorman 2012). They also find stronger vertical velocities in updrafts, though as pointed out in MOB11, the increase in vertical velocity w does not necessarily imply an increase in vertical mass flux ρw . The latter is more relevant to precipitation extremes.

The above results were derived in disorganized convection. Nevertheless, convective organization can strongly impact the distribution of precipitation and convective properties, and a large fraction of precipitation extremes occurs in organized convection. Various mechanisms can generate and modulate convective organization, such as internal feedbacks involving water vapor (Held et al. 1993; Tompkins 2001) or radiation (Bretherton et al. 2005; Stephens et al. 2008; Muller and Held 2012), as well as external forcings such as background vertical shear (Rotunno et al. 1988; Fovell and Ogura 1988; Garner and Thorpe 1992; Weisman and Rotunno 2004; Robe and Emanuel 2001). The ubiquity of convective organization above tropical oceans has been pointed out in several observational studies (Houze and Betts 1981; WCRP 1999; Nesbitt et al. 2000).

Recent results from Singleton and Toumi (2012) indicate that changes in precipitation extremes could be significantly larger when the convection is organized. Using a high-resolution CRM to study the response of precipitation extremes to warming in an idealized squall line,

they find precipitation extremes changes in excess of CC (at surface temperatures higher than 24°C), due to stronger vertical mass fluxes with warming. Though this study raises the possibility that organized convection could yield stronger amplifications of extremes, the warming in this case was done by warming the atmosphere by one degree uniformly in the vertical. A uniform vertical warming increases the atmospheric instability. Indeed the change of temperature consistent with a warmer moist adiabat, as is expected in response to an SST increase in the tropics, yields stronger warming aloft than at low levels. The increased atmospheric instability with uniform vertical warming could potentially overestimate the increase in vertical velocities and mass fluxes, and hence the amplification of precipitation extremes.

The goal of this paper is to investigate the response of precipitation extremes to an SST increase in a CRM with organized convection. Background vertical shear is used to organize the convection into squall lines. The shear is maintained through the simulations which are run to radiative convective equilibrium. Once equilibrium is reached, we start our analysis. Note that this is a slightly different setting than Singleton and Toumi (2012) who fix the background state and let the squall line propagate through this imposed background state. In our simulations on the other hand, the squall line is in equilibrium with the mean state. Although our setting is idealized (square, doubly-periodic domain over ocean, no large scale forcing, no orography), it can help shed some light on the impact of convective organization on the amplification of precipitation extremes with warming, and the methodology developed should also be applicable to less idealized simulations. Of particular interest are the following questions:

- Without convective organization it was found in cloud-resolving simulations that the fractional increase in precipitation extremes was substantially smaller than that in atmospheric water vapor, and was closer to the increase in surface water vapor concentrations. Does this result still hold in organized convection? Or does convective organization yield stronger amplifications of precipitation extremes with warming?

- Is the response of precipitation extremes to warming monotonic in the strength of the background vertical shear applied? In other words, does stronger shear yield larger amplifications?
- Can we use the framework introduced in MOB11 to investigate the thermodynamic and dynamic contributions to changes in precipitation extremes with warming? Can it help explain the sensitivity to shear?

The next section describes the numerical experiments, which are also listed in Table 1. Section §3 examines the response of mean precipitation to warming for different shear values. Section §4 describes the response of precipitation extremes, which are analyzed further in §5 using an approximate scaling for precipitation extremes. Conclusions are offered in §6.

2. Numerical simulations

The CRM used in this study is the System for Atmospheric Modeling, or SAM [version 6.6; see Khairoutdinov and Randall (2003) for a full description]. The model solves the anelastic continuity, momentum and tracer conservation equations. The prognostic thermodynamic variables of the model include total non-precipitating water (vapor + cloud water + cloud ice) and total precipitating water (rain + snow + graupel). The mixing ratio of cloud water, cloud ice, rain, graupel and snow are diagnosed from the prognostic variables using a temperature dependent partition between liquid and ice phases. The frozen moist static energy, which is the sum of the liquid/ice water static energy and the total condensate amount times the latent heat of vaporization, is conserved during moist adiabatic processes in the model, including the freezing and melting of precipitation. The model is run to radiative convective equilibrium, and once equilibrium is reached the precipitation extremes are analyzed.

All simulations are three-dimensional on a square, doubly-periodic horizontal domain. The vertical grid has 64 levels (capped at 27 km with a rigid lid) with the first level at 37.5

m and grid spacing gradually increasing from 80 m near the surface to 400 m above 5 km, and a variable time step (10 s or less to satisfy the Courant/Friedrichs/Lewy condition). The surface fluxes are computed using Monin-Obukhov similarity. To reduce gravity wave reflection and buildup, Newtonian damping is applied to all prognostic variables in the upper third of the model domain. We run three cases: the control case CTRL with resolution $dx = 1$ km and domain size $L = 256$ km; the small domain case SMLDMN with the same resolution as CTRL but a smaller domain size $L = 128$ km; and the low resolution case LOWRES with the same domain size as CTRL but a coarser resolution $dx = 2$ km (see Table 1 for a summary of the various simulations).

For all those three cases, we perform two experiments: the cold experiment with an SST of 300 K, and the warm experiment with an SST of 302 K. The radiative cooling rates are fixed for convenience (smaller computational costs) and because we empirically found it easier to generate squall lines with fixed radiative cooling rates in this model. MOB11 showed that it is important to allow the radiative cooling profile to change according to the SST in warming experiments. This is because all vertical profiles shift upward following the warmer moist adiabat, and the radiative cooling profile needs to shift upward accordingly. Otherwise the detrainment level is too low in the warm experiment (Hartmann and Larson 2002), and one obtains unrealistic decreases in condensate amounts and increases in precipitation efficiency. Therefore we use different radiative cooling profiles in the cold and warm experiments (whose profiles are given on Fig. 1), which are obtained from a smaller domain run with interactive radiation and with the corresponding SSTs.

Vertical shear is imposed to organize the convection into squall lines. It is well known that in the presence of vertical wind shear, convection organizes into lines. This organization follows from the fact that the background shear opposes the displacement of the cold pool and associated gust front relative to the free convection (e.g., Rotunno et al. (1988); Fovell and Ogura (1988); Garner and Thorpe (1992); Weisman and Rotunno (2004)). Three shear profiles are used: zero shear (“Shear0”), critical shear (“Shear1”) and supercritical shear

(“Shear2”). The shear profiles are shown on the left panels of Fig. 2. The mean wind is relaxed over a time scale of two hours toward these wind profiles. The critical shear corresponds to squall lines perpendicular to the shear (the shear is in the x direction in all our simulations), and is empirically determined to decrease from $U = 10 \text{ m s}^{-1}$ at the surface to $U = 0 \text{ m s}^{-1}$ at 1 km. The supercritical shear, which is obtained by doubling the critical shear, yields squall lines oriented at an angle of about 45° with respect to the shear, so that the projection of the shear onto the squall line is critical (see e.g. Robe and Emanuel (2001)). The right panels of Fig. 2 show snapshots of clouds in the CTRL case with the three different shear profiles.

The organization looks similar in all three cases (CTRL, SMLDMN and LOWRES), as can be seen on Fig. 3, 4 and Fig. 5 which show time series of instantaneous vertically-integrated atmospheric water vapor in all cases without shear, with critical shear and with supercritical shear respectively. Without shear (Fig. 3), convection is disorganized. Individual convective events occur somewhat randomly throughout the domain and typically last a few hours (the snapshots in Fig. 3 are separated by an hour). With critical shear (Fig. 4), the simulation looks quite different. All the convection is aligned along a squall line perpendicular to the shear, and the line is very steady in time (the snapshots in Fig. 4 are separated by a day and a half). With supercritical shear (Fig. 5), the convecting line is oriented at an angle of about 45° , so that the cross-line component of shear is near its critical value. The lines are slowly advected downshear (the snapshots in Fig. 5 are separated by five hours), at a rate of about 2 m s^{-1} which is much slower than the surface background velocity (20 m s^{-1}).

Table 1 summarizes the various simulations. We now investigate the change in the distribution of precipitation, mean and extremes, between the cold run and the warm run in the various cases for different shears.

3. Results: mean precipitation

The time and space mean precipitation satisfies the mean energy budget of the atmosphere:

$$L_v \langle P \rangle + \langle S \rangle \approx \langle Q_{rad} \rangle, \quad (1)$$

where $L_v P$ is the latent heat associated with the surface precipitation P , S is the surface sensible heat flux, Q_{rad} the vertically integrated radiative cooling, and $\langle . \rangle$ denotes time and space average. Since we use fixed radiative cooling rates, the change in radiative cooling is the same in all cases and for all shears. Therefore we expect the change in mean precipitation to be similar in all the runs modulo some small changes in S . We see that this is indeed the case: Fig.6 shows the changes in mean precipitation, precipitation intensity (defined as the precipitation averaged over points with non-zero precipitation), precipitation frequency (frequency of occurrence of non-zero precipitation), precipitable water and near-surface specific humidity (at the first model level $z = 37.5$ m). The change in surface water vapor is always smaller than the change in atmospheric water vapor for two reasons: first, on a warmer moist adiabat, the warming is stronger aloft than at low levels; second the fractional rate of increase as predicted by the CC equation at fixed relative humidity depends on temperature and increases at lower temperatures, hence at higher altitudes.

The changes in mean precipitation are approximately the same in all cases, consistent with the energetic constraint and the observed small changes in surface sensible heat flux (not shown). More importantly, changes in mean precipitation are smaller than the increase in atmospheric moisture, or CC scaling. This is consistent with the fact that mean precipitation is determined by energetics, not by local thermodynamics. The changes in precipitation intensity are also smaller than CC, and generally even smaller than CC_{sfc} except with the strongest shear at low resolution. In that case, the precipitation frequency decreases significantly (-3.4% K^{-1}), which allows for a larger increase in precipitation intensity (keeping the change in mean precipitation fixed). The decrease in precipitation frequency with super-

critical shear is robust throughout all the cases, but the strongest decrease at low resolution might be an artefact of the coarse resolution.

The small increases in precipitation intensity in our simulations are at odds with results from Singleton and Toumi (2012) who find a $1.5 \times \text{CC}$ increase in storm-averaged rainfall. This might be the consequence of the uniform vertical warming that they use, which increases the atmospheric instability and hence likely overestimates vertical velocities in updrafts.

4. Results: precipitation extremes

We now investigate the change in the distribution of hourly-mean pointwise precipitation, with particular emphasis on the change in its extremes. The extremes are computed over all times and all points in space. We checked the convergence of the precipitation extremes in our simulations by splitting the time series in two and comparing the extremes obtained in the two subsamples. We find that the convergence of extremes is much faster (typically a few days) without shear than with shear (tens of days), probably due to more internal variability with shear. Our analysis therefore required long simulations, 40 days in CTRL and 52 days in SMLDMN and LOWRES (the convergence is slightly faster in CTRL which has the largest number of points).

In order to initiate our study of precipitation extremes, we compute the distribution of precipitation in the control case CTRL. Precipitation rates as a function of percentile in the cold and warm simulations are shown in the top panel of Fig. 7. We see that precipitation extremes are sensitive to vertical shear, and almost double in the presence of shear. But interestingly, increasing the shear from critical to supercritical shear has very little effect on the rainfall rates. This is a robust result throughout all our cases (not shown): adding a background vertical shear strongly impacts the high percentiles of precipitation, but the value of the shear, critical or supercritical, has little impact.

We also see from Fig. 7 that warming yields larger precipitation rates at the highest

percentiles. This is even clearer in the lower panel which shows the fractional increase in precipitation extremes accompanying the SST increase. Despite very different precipitation values and convective organizations, the response to warming is similar for all shears: the fractional increase in precipitation extremes converges at the highest percentiles, to a value of about 10 % for Shear0 and Shear1, and to a higher value of about 15 % for Shear2.

A similar computation can be done in all the cases, CTRL SMLDMN and LOWRES, and the results are summarized on Fig. 8. The changes in atmospheric (PW) and in near-surface (q_{vsfc}) water vapor are also shown as gray lines for reference (CC and CC_{sfc} scalings respectively). We see that the exact value of the fractional increase in precipitation extremes is somewhat sensitive to the domain size and resolution, but there are several robust features. First, in all the cases and shears, the increase in precipitation extremes is significantly smaller than the increase in atmospheric humidity. Second, despite the very different convective organizations without shear and with critical shear (Figs. 3 and 4), the response of precipitation extremes to warming is surprisingly similar, with a rate of increase much smaller than CC and even slightly smaller than CC_{sfc} . Third, the extremes have a stronger response to warming with supercritical shear. Extremes can increase at a rate close to or even above CC_{sfc} .

Our results without shear are consistent with MOB11 who find that in disorganized convection, the fractional increases in precipitation extremes are substantially less than the fractional increases in column water vapor, and are comparable in magnitude to (and slightly smaller than) those in surface water vapor concentrations (see their Fig. 4). But our results with organized convection are at odds with Singleton and Toumi (2012) who find greater fractional rates of increase than the amount of atmospheric water vapor in their simulated squall lines. As noted earlier, we interpret their result as being the consequence of the uniform vertical warming which increases the atmospheric instability and hence likely overestimates vertical velocities in updrafts.

Singleton and Toumi (2012) also observe a change in the behaviour of extremes at an

288 SST of 24° C, with larger rates of increase for SSTs above 24° C. According to their Fig. 1,
 289 this SST corresponds to a transition between stationary squall lines (near-critical shear) and
 290 slanted squall lines (supercritical shear), which could explain the change of behaviour of
 291 extremes. It is interesting that the response of extremes to warming is not monotonic with
 292 shear, and is mainly sensitive to the strongest supercritical shear in our simulations. As we
 293 will see in the next section, this is related to the behaviour of vertical velocities in updrafts
 294 which respond differently to warming with critical and with supercritical shears. Singleton
 295 and Toumi (2012) also note that vertical velocities play a role in the super CC scalings that
 296 they observe. In the next section we use a simple expression to analyze further those results
 297 and examine the thermodynamic and dynamic contributions to the changes in precipitation
 298 extremes in our simulations.

299 **5. Scaling for changes in precipitation extremes**

300 *a. Scaling*

301 Our goal is to relate changes in precipitation extremes to changes in dynamic and ther-
 302 modynamic variables. To that end, we use an approximate expression, or scaling, for the
 303 precipitation rate in an extreme precipitation event. Following MOB11, we use an energy
 304 rather than a water budget to derive the scaling, because an energy budget allows us to more
 305 easily define a thermodynamic component (with no dependence on relative humidity), and
 306 also because the weak horizontal gradients of temperature in the tropics help to eliminate
 307 horizontal advective terms. From the vertically integrated dry static energy (DSE) budget
 308 of the model (Khairoutdinov and Randall 2003), it can be shown that the precipitation rate
 309 in an extreme event, P_e , is approximately given by (MOB11)

$$310 \quad P_e = \epsilon \frac{1}{L_v} \int \bar{\rho} w \frac{\partial \langle s \rangle}{\partial z}, \quad (2)$$

where ϵ denotes precipitation efficiency as defined in MOB11, L_v latent heat of evaporation, $\bar{\rho}$ reference density profile used in the anelastic governing equations, w resolved wind speeds along the Cartesian direction z , $s = c_p T + gz$ dry static energy, $\langle . \rangle$ domain and time mean, and the integral is given by

$$\int (\dots) = \int_{900 \text{ hPa}}^{150 \text{ hPa}} (\dots) dz.$$

Note that this scaling is similar but not identical to the one used in MOB11 in two ways: first the integration bounds are not exactly the same. The lower and upper boundaries for the vertical integral are introduced to exclude the subcloud layer (see the mean profiles of non-precipitating condensates on Fig. 9) and top layers of the model where damping is applied to avoid gravity wave reflection and build up; we conducted the same analysis changing the lower and upper boundaries by ± 50 hPa and found that our results are not sensitive to those values. Second, MOB11 use the fact that the mean atmospheric lapse rate is close to moist adiabatic in the model above the boundary layer (i.e. $ds \approx -L_v dq_{sat}$) to express the scaling (2) in terms of the saturation specific humidity from the mean temperature $q_{sat}(\langle T \rangle)$ instead of mean dry static energy $\langle s \rangle$. This makes the interpretation of the scaling easier, since

$$\int \bar{\rho} w \frac{-\partial q_{sat}(\langle T \rangle)}{\partial z}$$

is simply the net condensation in the atmospheric column, including condensation from upward motion as well as evaporation of condensates from downward motion, maintaining a moist adiabatic lapse rate. We do not take this extra step because we find that with shear, the agreement with precipitation extremes is better when we use the mean dry static energy, although the qualitative results are unchanged when using saturation specific humidity. We will come back to the interpretation of the scaling and its relationship to water vapor in §5c.

If changes in the precipitation efficiency are neglected, then from (2) fractional changes in P_e are given by the scaling relation:

$$\frac{\delta P_e}{P_e} \approx \frac{\delta \int \bar{\rho} w (\partial \langle s \rangle / \partial z)}{\int \bar{\rho} w (\partial \langle s \rangle / \partial z)}. \quad (3)$$

The fractional changes in the scaling (3) with various shears in the CTRL case are shown on the middle panel of Fig. 10. The other cases (SMLDMN and LOWRES) look similar. In fact, all the results discussed here and in the following sections hold in all the cases, therefore, from now on, we only show results for the CTRL case. To ease comparison, we repeated the precipitation extremes changes from Fig. 8 on the left panel of Fig. 10. We see that the scaling captures the magnitude of the rate of increase of precipitation extremes with warming, as well as its sensitivity to shear: the amplification of extremes is similar without shear and with critical shear, and is larger with supercritical shear. In the next section, we use the scaling (3) to evaluate the thermodynamic and dynamic contributions to precipitation extremes changes.

b. Thermodynamic and dynamic contributions

We can further decompose the scaling into two components, a thermodynamic component involving the change in dry static stability $\delta(\partial < s > / \partial z)$, and a dynamic component involving the change in upward mass flux $\delta \bar{\rho} w$ (neglecting second order terms):

$$\delta \left(\int \bar{\rho} w \frac{\partial < s >}{\partial z} \right) \approx \int \bar{\rho} w \delta \left(\frac{\partial < s >}{\partial z} \right) + \int \delta(\bar{\rho} w) \frac{\partial < s >}{\partial z}. \quad (4)$$

The right panel of Fig. 10 shows the thermodynamic and dynamic contributions to the scaling. We see that to first order, the rate of increase of precipitation extremes has the same magnitude as the thermodynamic scaling, which has a similar value for all shears, smaller than CC and close to $CC_{\text{sfc}} \approx 6 - 7 \% \text{ K}^{-1}$. This value is consistent with the mean fractional increase of dry static stability $\partial < s > / \partial z$ averaged over the cloudy layers (900 to 150 hPa from Fig. 9) on a theoretical moist adiabat when the SST is increased from 300 to 302 K; see also the values given by Betts and Harshvardhan (1987). The dynamic contribution on the other hand is not the same for all shears. It is small compared to the thermodynamic scaling, but it can vary greatly with shear. In fact, Fig. 10 makes clear that the larger amplifications of extremes with supercritical shear are due to positive dynamic contributions, as opposed

to negative dynamic contributions without shear and with critical shear.

To summarize these results, to first order the changes in precipitation extremes are captured by changes in the mean temperature structure of the atmosphere. This thermodynamic contribution is robust for all shears and is close to $CC_{\text{sfc}} \approx 6 - 7 \text{ \% K}^{-1}$, which is significantly smaller than the change in atmospheric water vapor $CC \approx 9 - 10 \text{ \% K}^{-1}$. Changes in convective mass fluxes play a secondary role, and are not robust to shear. They tend to weaken the strength of precipitation extremes without shear and with critical shear, while they tend to increase the strength of precipitation extremes with supercritical shear.

c. Relationship to water vapor

In order to clarify the relationship between the scaling (3) and near-surface water vapor, we derive an even simpler scaling for the changes in precipitation extremes. While not as accurate as (3), it helps explain why changes in precipitation extremes follow CC_{sfc} . Since the tropical atmosphere is close to a moist adiabat, i.e. $ds \approx -L_v dq_{\text{sat}}$, and since changes in relative humidity tend to be small, i.e. $\delta(\partial q_{\text{sat}}/\partial z) \approx \delta(\partial q_v/\partial z)$ where q_v denotes water vapor specific humidity, it follows from (3) that

$$\frac{\delta P_e}{P_e} \approx \frac{\delta \int \bar{\rho} w (-\partial \langle q_v \rangle / \partial z)}{\int \bar{\rho} w (-\partial \langle q_v \rangle / \partial z)}. \quad (5)$$

If we further assume that a representative value of $\bar{\rho} w$ is its value at 500 hPa (around 6 km), then a rough scaling would be:

$$\int \bar{\rho} w \left(-\frac{\partial \langle q_v \rangle}{\partial z} \right) \sim (\bar{\rho} w)_{500} \int -\frac{\partial \langle q_v \rangle}{\partial z} = \delta(\bar{\rho} w)_{500} \langle q_v \rangle_{BL}. \quad (6)$$

An alternative way to derive this scaling is to assume that in areas with strong convection, the precipitation is equal to the total water vapor horizontal convergence in the boundary layer

$$P_e \sim \nabla_h(\bar{\rho} u_h)_{BL} \langle q_v \rangle_{BL}.$$

From mass conservation, the horizontal convergence in the boundary layer is equal to the vertical mass flux in the convective updraft $\nabla_h(\bar{\rho} u_h)_{BL} \approx (\bar{\rho} w)_{500}$, so that precipitation

extremes scale with

$$P_e \sim (\bar{\rho}w)_{500} < q_v >_{BL} . \quad (7)$$

The fractional changes in the scaling (7) are shown on the middle panel of Fig. 11, and the thermodynamic and dynamic contributions ($\delta < q_v >_{BL} / < q_v >_{BL}$ and $\delta(\bar{\rho}w)_{500}/(\bar{\rho}w)_{500}$ respectively) are shown on the right panel. While not as accurate as (3), this rough scaling captures the general behaviour of precipitation with warming. To leading order, the magnitude of the amplification of extremes with warming scales with boundary layer water vapor, and is robust throughout all cases and shears. Changes in convective mass fluxes play a secondary role, and unlike the earlier dynamic contributions in (4), they tend to weaken precipitation extremes for all shears. The weakening is stronger without shear and with critical shear than it is with supercritical shear, which explains the larger rates of increase of (7) with supercritical shear.

The top panels of Fig. 12 show the vertical profiles of mass flux at the 99.95th precipitation percentile in the control case for the various shears (the other cases look similar). Consistent with the dynamic contributions described earlier, we see that the decrease in vertical mass fluxes with critical and zero shear is not observed with supercritical shear. The decrease in vertical mass flux with zero shear is not inconsistent with Romps (2011) and MOB11 who find an increase in updraft velocities with warming in disorganized convection. Fig. 12 shows that the decrease in convective mass flux occurs despite an increase in the maximum updraft velocity (bottom panels). The former is more relevant to precipitation extremes.

It is unclear why the decrease in mass flux at high precipitation percentiles does not occur in the presence of supercritical shear. Note that the change in mean mass flux M , which can be estimated from the mean precipitation and near-surface specific humidity changes (shown on Fig. 6) $\delta M/M \approx \delta P/P - \delta q_{vsfc}/q_{vsfc}$ (Betts 1998; Held and Soden 2006), is approximately the same for all cases and shears, and decreases at a rate of about 3 - 4 % K⁻¹. The discrepancy between the decrease in mean convective mass flux, which is the same for all shears, and the decrease in convective mass flux at high precipitation percentiles, which does

not occur with supercritical shear, may be related to the decrease in precipitation frequency with supercritical shear discussed in §3 (less convective events with the same individual mass fluxes yield a smaller mean mass flux). Given its impact on precipitation extremes, more work is desirable to investigate in detail the distribution of convective mass flux and its response to warming.

6. Conclusions

Earlier studies of disorganized radiative-convective equilibrium found that the fractional rate of increase of precipitation extremes with warming were close to that of surface water vapor concentrations, or CC_{sfc} scaling, which is substantially less than the fractional increase in column water vapor, or CC scaling (Romps (2011), MOB11). Recent results from Singleton and Toumi (2012) indicate that changes in precipitation extremes could be significantly larger when the convection is organized.

Using vertical shear to organize the convection into squall lines, we examine the response of precipitation extremes to warming in a CRM. Several shear profiles are investigated, namely no shear, critical shear and supercritical shear, as well as various domain sizes and resolutions. We find that the exact value of the increase in precipitation extremes with warming is somewhat sensitive to resolution and domain size, but there are several robust features:

- Regardless of the strength of the shear, the fractional rate of increase of precipitation extremes with warming is comparable in magnitude to that of surface water vapor concentrations, which is significantly smaller than the increase in column water vapor.
- Despite very different convective organizations (compare Figs. 3 and 4), the amplification of precipitation extremes without shear and with critical shear are surprisingly similar, with a rate of increase slightly smaller than CC_{sfc} . The dependence on shear is non-monotonic and extremes are more sensitive to supercritical shear which yields

increases close to or slightly above CC_{sfc} .

- An approximate scaling is used to identify thermodynamic and dynamic contributions to precipitation extremes. We find that for all shears, to first order the amplification of extremes is dominated by the thermodynamic component which is close to CC_{sfc} and is related to changes in the mean temperature structure of the atmosphere. The dynamic contributions play a secondary role, and differ for different shears: without shear and with critical shear the dynamic component tends to weaken extremes, while with supercritical shear it strengthens extremes.

The dynamic contribution is small but is responsible for the different behaviours with different shears. These are caused by different responses of convective mass fluxes in individual updrafts: the decrease in mass fluxes at high precipitation percentiles with warming observed with zero and critical shear is not observed with supercritical shear (note that mass fluxes decrease with warming despite an intensification of maximum updraft velocities).

This is consistent with MOB11 who find that without organization, the changes in precipitation extremes are closer to (and slightly below) CC_{sfc} than to CC , and are captured to first order by changes in the mean temperature structure of the atmosphere; they also find that changes in vertical velocities play a secondary role and tend to weaken the strength of precipitation extremes, despite an intensification of updraft velocities in the upper troposphere. But with organization, our results are at odds with Singleton and Toumi (2012) who find precipitation extremes increases in excess of CC . We interpret their result as being the consequence of the uniform vertical warming which increases the atmospheric instability and hence likely overestimates vertical velocities and mass fluxes in updrafts, and hence precipitation extremes. Interestingly, Singleton and Toumi (2012) observe a change of behaviour of precipitation extremes in their simulated squall line when the SST exceeds 24°C . Our results indicate that this might be due to the fact that this SST corresponds to a transition between stationary squall lines (near-critical shear) and slanted squall lines (supercritical shear), which could explain the change of behaviour of extremes.

In the tropics, using column water vapor as a proxy for the rate of change of precipitation extremes instead of surface humidity can lead to substantial overestimates. Although our setting was idealized (square, doubly-periodic domain, fixed radiative cooling rates and SSTs, no large scale forcing or orography), the methodology developed should also be applicable to less idealized simulations. More work is desirable to investigate whether changes in precipitation extremes larger than those in atmospheric water vapor are possible under more realistic conditions.

Acknowledgments.

The author would like to thank Isaac Held and Steve Garner for useful discussions about this work, as well as Andrew Singleton and Ralf Toumi for providing further details about their simulations. Financial support for this work under the U.S. Department of Energy Grant DE-SC0006841 is gratefully acknowledged.

REFERENCES

- 480 Allan, R. P. and B. J. Soden, 2008: Atmospheric warming and the amplification of precipi-
481 tation extremes. *Science*, **321** (5895), 1481.
- 482 Allen, M. R. and W. J. Ingram, 2002: Constraints on future changes in climate and the
483 hydrologic cycle. *Nature*, **419**, 224–232.
- 484 Betts, A. K., 1998: Climate-convection feedbacks: Some further issues. *Climatic Change*,
485 **39**, 35–38.
- 486 Betts, A. K. and Harshvardhan, 1987: Thermodynamic constraint on the cloud liquid water
487 feedback in climate models. *J. Geophys. Res.*, **92** (7), 8483–8485.
- 488 Bretherton, C. S., P. N. Blossey, and M. Khairoutdinov, 2005: An energy-balance analysis of
489 deep convective self-aggregation above uniform SST. *J. Atmos. Sci.*, **62** (12), 4273–4292.
- 490 Emori, S. and S. J. Brown, 2005: Dynamic and thermodynamic changes in mean and extreme
491 precipitation under changed climate. *Geophys. Res. Lett.*, **32**, L17 706.
- 492 Fovell, R. G. and Y. Ogura, 1988: Numerical simulation of a midlatitude squall line in two
493 dimensions. *J. Atmos. Sci.*, **45** (24), 3846–3879.
- 494 Garner, S. T. and A. J. Thorpe, 1992: The development of organized convection in a sim-
495 plified squall-line model. *Quart. J. Roy. Meteor. Soc.*, **118** (503), 101–124.
- 496 Hartmann, D. L. and K. Larson, 2002: An important constraint on tropical cloud–climate
497 feedback. *Geophys. Res. Lett.*, **29**, 1951.
- 498 Held, I. M., R. S. Hemler, and V. Ramaswamy, 1993: Radiative-convective equilibrium with
499 explicit two-dimensional moist convection. *J. Atmos. Sci.*, **50** (23), 3909–3909.

500 Held, I. M. and B. J. Soden, 2006: Robust Responses of the Hydrological Cycle to Global
501 Warming. *J. Climate*, **19**, 5686–5699.

502 Houze, R. A., Jr. and A. K. Betts, 1981: Convection in gate. *Rev. of Geophys. Space Phys.*,
503 **19 (4)**, 541–576.

504 Khairoutdinov, M. F. and D. A. Randall, 2003: Cloud-resolving modeling of the arm summer
505 1997 iop: Model formulation, results, uncertainties and sensitivities. *J. Atmos. Sci.*, **60**,
506 607–625.

507 Kharin, V. V., F. W. Zwiers, X. Zhang, and G. C. Hegerl, 2007: Changes in temperature
508 and precipitation extremes in the ipcc ensemble of global coupled model simulations. *J.*
509 *Climate*, **20**, 1419–1444.

510 Lenderink, G., H. Y. Mok, T. C. Lee, , and G. J. van Oldenborgh, 2011: Scaling and
511 trends of hourly precipitation extremes in two different climate zones - hong kong and the
512 netherlands. *Hydrol. Earth Syst. Sci.*, **15**, 3033–3041.

513 Lenderink, G. and E. van Meijgaard, 2008: Increase in hourly precipitation extremes beyond
514 expectations from temperature changes. *Nature Geosci.*, **1**, 511–514.

515 Liu, S. C., C. Fu, C.-J. Shiu, J.-P. Chen, and W. F., 2009: Temperature dependence of
516 global precipitation extremes. *Geophys. Res. Lett.*, **36**, L17702.

517 Muller, C. J. and I. M. Held, 2012: Detailed investigation of the self-aggregation of convection
518 in cloud-resolving simulations. *J. Atmos. Sci. (in press)*.

519 Muller, C. J. and P. A. O’Gorman, 2011: An energetic perspective on the regional response
520 of precipitation to climate change. *Nature Climate Change*, **1 (5)**, 266–271.

521 Muller, C. J., P. A. O’Gorman, and L. E. Back, 2011: Intensification of precipitation extremes
522 with warming in a cloud-resolving model. *J. Climate*, **24 (11)**, 2784–2800.

523 Nesbitt, S. W., E. J. Zipser, and D. J. Cecil, 2000: A census of precipitation features in
524 the tropics using trmm: Radar, ice scattering, and lightning observations. *J. Climate*,
525 **13 (23)**, 4087–4106.

526 O’Gorman, P. A. and C. J. Muller, 2010: How closely do changes in surface and column
527 water vapor follow Clausius-Clapeyron scaling in climate-change simulations? *Environ.*
528 *Res. Lett.*, **5**, 025 207.

529 O’Gorman, P. A. and T. Schneider, 2009: The physical basis for increases in precipitation
530 extremes in simulations of 21st-century climate change. *Proc. Nat. Acad. Sci.*, **106**, 14 773–
531 14 777.

532 Pall, P., M. R. Allen, and D. A. Stone, 2007: Testing the Clausius-Clapeyron constraint on
533 changes in extreme precipitation under CO2 warming. *Clim. Dynam.*, **28**, 351–363.

534 Robe, F. R. and K. A. Emanuel, 2001: The effect of vertical wind shear on radiative-
535 convective equilibrium states. *J. Atmos. Sci.*, **58 (11)**, 1427–1445.

536 Romps, D. M., 2011: Response of tropical precipitation to global warming. *J. Atmos. Sci.*,
537 **68 (1)**, 123–138.

538 Rotunno, R., J. B. Klemp, and M. L. Weisman, 1988: A theory for strong, long-lived squall
539 lines. *J. Atmos. Sci.*, **45 (3)**, 463–4.

540 Singh, M. S. and P. A. O’Gorman, 2012: Upward shift of the atmospheric general circulation
541 under global warming: theory and simulations. *J. Climate (in press)*.

542 Singleton, A. and R. Toumi, 2012: Super clausius-clapeyron scaling of rainfall in a model
543 squall line. *Quart. J. Roy. Meteor. Soc.*

544 Soden, B. J. and I. M. Held, 2006: An assessment of climate feedbacks in coupled ocean-
545 atmosphere models. *J. Climate*, **19 (14)**, 3354–3360.

- 546 Stephens, G. L., S. Van Den Heever, and L. Pakula, 2008: Radiative–convective feedbacks
547 in idealized states of radiative–convective equilibrium. *J. Atmos. Sci.*, **65**, 3899–3916.
- 548 Sugiyama, M., H. Shiogama, and S. Emori, 2010: Precipitation extreme changes exceeding
549 moisture content increases in MIROC and IPCC climate models. *Proc. Nat. Acad. Sci.*,
550 **107**, 571–575.
- 551 Tompkins, A. M., 2001: Organization of tropical convection in low vertical wind shears: The
552 role of water vapor. *J. Atmos. Sci.*, **58**, 529–545.
- 553 Trenberth, K. E., 1999: Conceptual framework for changes of extremes of the hydrological
554 cycle with climate change. *Climatic Change*, **42**, 327–339.
- 555 Trenberth, K. E., 2011: Changes in precipitation with climate change. *Clim. Res.*, **47** (1),
556 123.
- 557 Vecchi, G. A. and B. J. Soden, 2007: Global warming and the weakening of the tropical
558 circulation. *J. Climate*, **20**, 4316–4340.
- 559 WCRP, 1999: Proceedings of a conference on the toga coupled ocean-atmosphere response
560 experiment (coare). *COARE-98*, WCRP-107, WMO Tech. Doc. 940, 416.
- 561 Weisman, M. L. and R. Rotunno, 2004: "a theory for strong long-lived squall lines" revisited.
562 *J. Atmos. Sci.*, **61** (4), 361–382.
- 563 Wilcox, E. M. and L. J. Donner, 2007: The frequency of extreme rain events in satellite
564 rain-rate estimates and an atmospheric general circulation model. *J. Climate*, **20**, 53–69.

List of Tables

1	Description of the numerical simulations. The profiles of the various shears (zero shear = Shear0, critical shear = Shear1 and supercritical shear = Shear2) are shown in Fig. 2. Each case and shear is run twice, first with a Sea Surface Temperature (SST) of 300 K, and second with an SST of 302 K.	25
---	--	----

TABLE 1. Description of the numerical simulations. The profiles of the various shears (zero shear = Shear0, critical shear = Shear1 and supercritical shear = Shear2) are shown in Fig. 2. Each case and shear is run twice, first with a Sea Surface Temperature (SST) of 300 K, and second with an SST of 302 K.

case	shear	SST (K)	description
CTRL	Shear0	300	Control run (resolution 1 km, domain size 256 km) without shear and with SST = 300K.
		302	Same but SST = 302K.
	Shear1	300	Control run with critical shear and SST=300K.
		302	Same but SST = 302K.
	Shear2	300	Control run with supercritical shear and SST=300K.
		302	Same but SST = 302K.
SMLDMN	Shear0	300	Small domain run (resolution 1 km, domain size 128 km) without shear and with SST = 300K.
		302	Same but SST = 302K.
	Shear1	300	Small domain run with critical shear and SST = 300K.
		302	Same but SST = 302K.
	Shear2	300	Small domain run with supercritical shear and SST = 300K.
		302	Same but SST = 302K.
LOWRES	Shear0	300	Coarse resolution run (resolution 2 km, domain size 256 km) without shear and with SST = 300K.
		302	Same but SST = 302K.
	Shear1	300	Coarse resolution run with critical shear and SST = 300K.
		302	Same but SST = 302K.
	Shear2	300	Coarse resolution run with supercritical shear and SST = 300K.
		302	Same but SST = 302K.

List of Figures

- 1 Radiative cooling profiles used in the cold (SST=300K) and warm (SST=302K) simulations. The vertically integrated net atmospheric cooling increases from 94 W m⁻¹ to 101 W m⁻¹ with warming, yielding a 3.7 % K⁻¹ increase. 29
- 2 Snapshots of clouds (gray surfaces) and near-surface temperatures (first model level $z = 37.5$ m) in the CTRL runs with SST=300K (i.e. cold runs; the warm runs have similar organization) for various shears. The shears are shown on the left panels. Top panels: without shear, convection is not organized and resembles “pop-corn” convection. Middle panels: with critical shear (decreasing linearly from 10 m s⁻¹ at the surface to 0 at 1km), the convection organizes into a squall line perpendicular to the shear (the shear is in the x direction). Bottom panels: with supercritical shear (twice the critical shear), the lines are oriented at an angle of about 45°, so that the projected shear is critical. 30
- 3 Instantaneous precipitable water in the runs without shear and with SST=300K (the warm runs have similar organization). The snapshots on the left and right are separated by an hour. The top panels show the control run CTRL, the middle panels the small domain run SMLDMN, and the lower panels the coarse resolution run LOWRES (see Table 1 for a description of the runs). Without shear the convection is disorganized. 31
- 4 Same as Fig. 3 but with critical shear and with snapshots separated by a day and a half. With critical shear the convection is organized along lines perpendicular to the shear. 32
- 5 Same as Fig. 3 but with supercritical shear and with snapshots separated by five hours. With supercritical shear the convection is organized along lines oriented at an angle of about 45° with the shear. 33

595	6	Changes in mean precipitation, precipitation intensity, precipitation frequency,	
596		precipitable water and near-surface specific humidity (first model level $z =$	
597		37.5 m) in the various cases (see Table 1 for a description of the runs). All the	
598		quantities shown are changes in time-domain averages and are given in % K^{-1} .	34
599	7	Changes in the distribution of hourly mean pointwise precipitation accompa-	
600		nying a 2 K SST increase in the control case (CTRL see Table 1 for details)	
601		for various shears. The top panel shows the values of precipitation percentiles	
602		in $mm\ day^{-1}$ in the cold and warm simulations. The bottom panel shows the	
603		fractional increase in rainfall rates between those two runs.	35
604	8	Changes in the distribution of hourly mean pointwise precipitation accompa-	
605		nying a 2 K SST increase for various cases (CTRL, SMLDMN and LOWRES,	
606		see Table 1 for details) and shears. All the values are in %. The changes in	
607		precipitable water and near-surface specific humidity are shown as gray solid	
608		and dashed lines respectively. To ease comparison, the curves for various	
609		shears are superimposed on the right panels.	36
610	9	Vertical profiles of non-precipitating condensate amounts (i.e. clouds, in g	
611		kg^{-1}) in the control case, domain and time averaged, for various shears.	37
612	10	Changes in precipitation extremes (left panel), in the scaling (3) (middle	
613		panel) and in the dynamic and thermodynamic parts of the scaling (right	
614		panel) in the CTRL case. All the values are in %.	38
615	11	Same as Fig. 10, but the middle and right panels show changes in the rough	
616		estimate (7) $(\rho w)_{500} < q_v >_{BL}$ (where $< . >$ denotes time and spatial mean).	
617		Its thermodynamic part is $\delta < q_v >_{BL}$, and its dynamic part is $\delta(\rho w)_{500}$. All	
618		the values are in %.	39

12 Vertical mass flux (top panels) and vertical velocities (bottom panels) in the
control case at the 99.95th percentile of precipitation for various shears. The
values are shown on the left panels, and the changes between the cold and
warm runs are shown on the right panels.

40

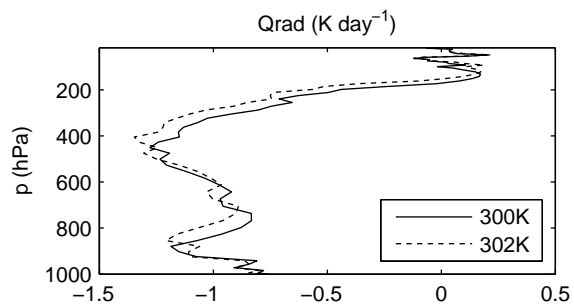


FIG. 1. Radiative cooling profiles used in the cold (SST=300K) and warm (SST=302K) simulations. The vertically integrated net atmospheric cooling increases from 94 W m^{-1} to 101 W m^{-1} with warming, yielding a 3.7 \% K^{-1} increase.

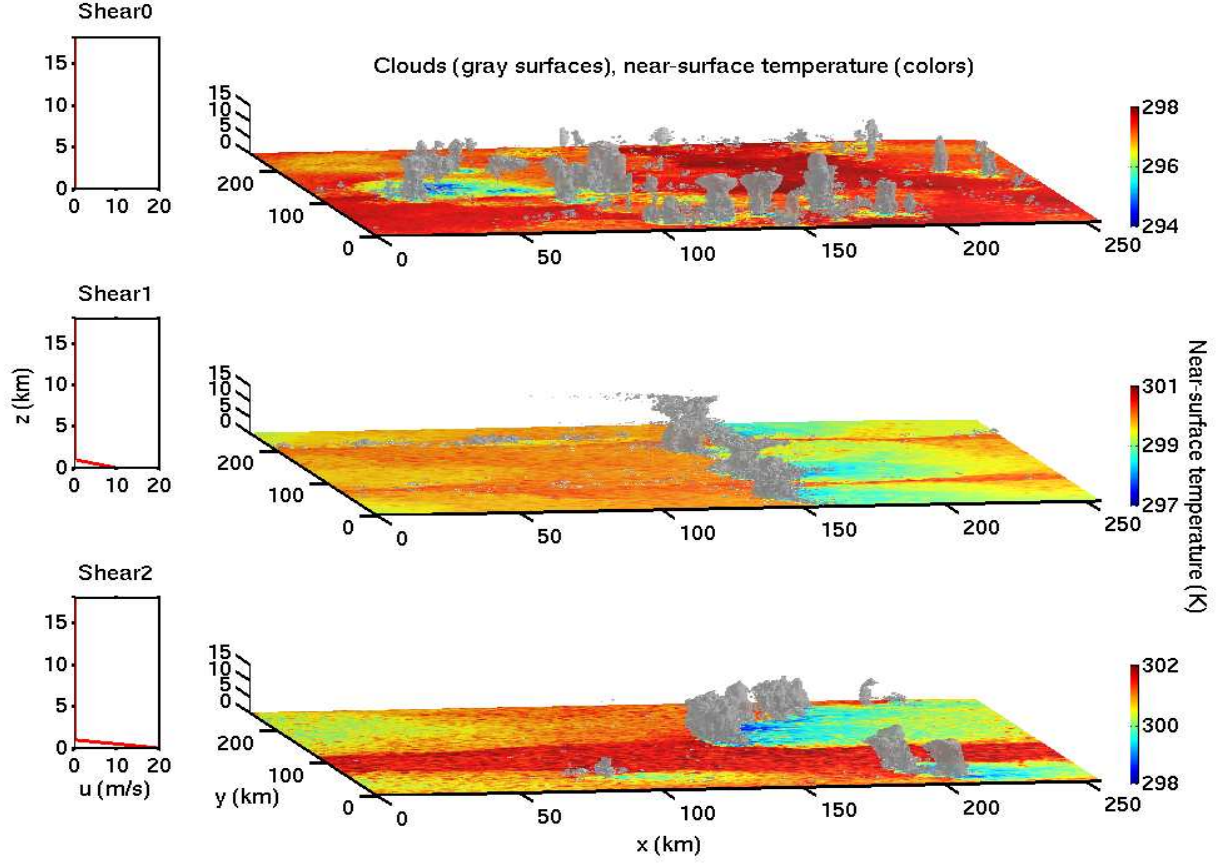


FIG. 2. Snapshots of clouds (gray surfaces) and near-surface temperatures (first model level $z = 37.5$ m) in the CTRL runs with SST=300K (i.e. cold runs; the warm runs have similar organization) for various shears. The shears are shown on the left panels. Top panels: without shear, convection is not organized and resembles “pop-corn” convection. Middle panels: with critical shear (decreasing linearly from 10 m s^{-1} at the surface to 0 at 1km), the convection organizes into a squall line perpendicular to the shear (the shear is in the x direction). Bottom panels: with supercritical shear (twice the critical shear), the lines are oriented at an angle of about 45° , so that the projected shear is critical.

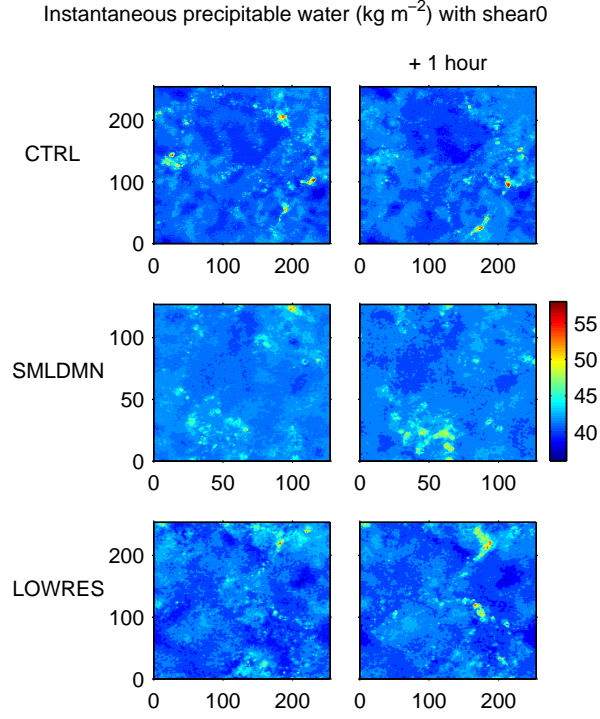


FIG. 3. Instantaneous precipitable water in the runs without shear and with $\text{SST}=300\text{K}$ (the warm runs have similar organization). The snapshots on the left and right are separated by an hour. The top panels show the control run CTRL, the middle panels the small domain run SMLDMN, and the lower panels the coarse resolution run LOWRES (see Table 1 for a description of the runs). Without shear the convection is disorganized.

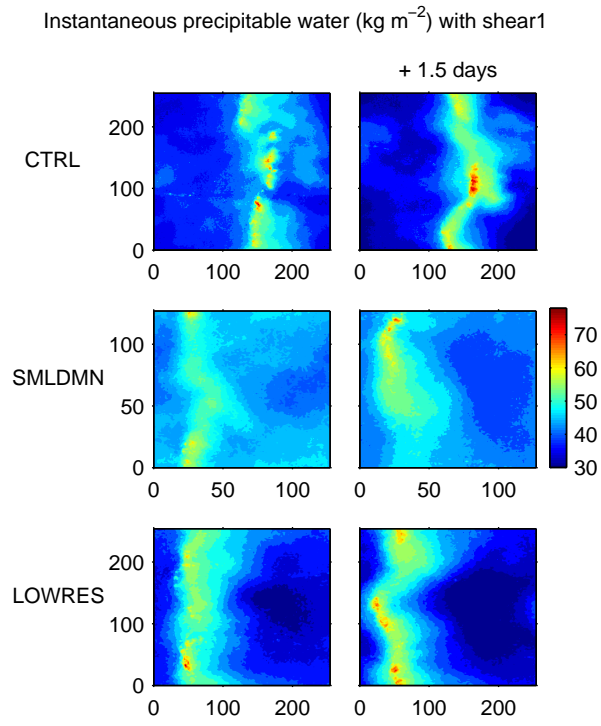


FIG. 4. Same as Fig. 3 but with critical shear and with snapshots separated by a day and a half. With critical shear the convection is organized along lines perpendicular to the shear.

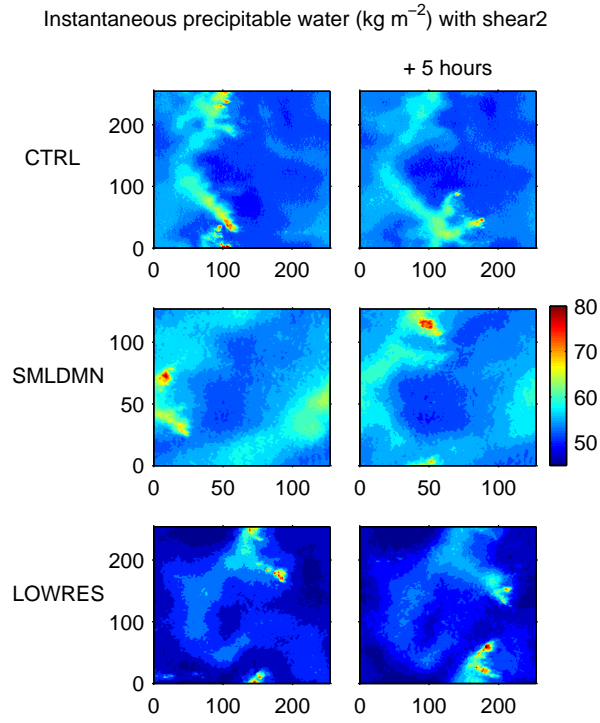


FIG. 5. Same as Fig. 3 but with supercritical shear and with snapshots separated by five hours. With supercritical shear the convection is organized along lines oriented at an angle of about 45° with the shear.

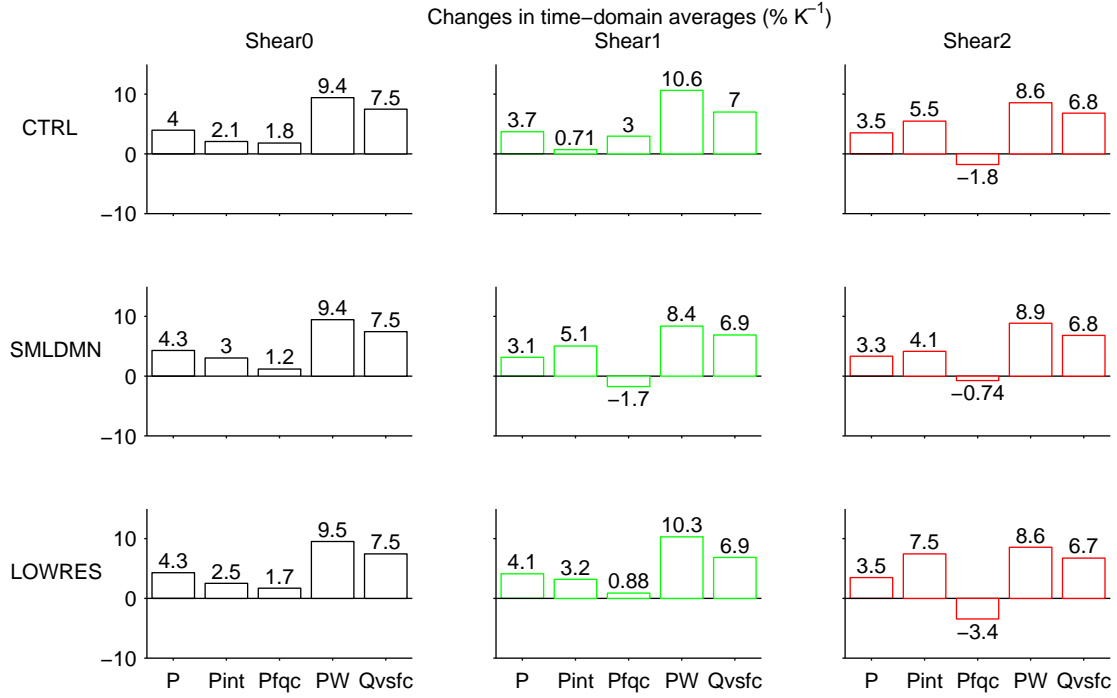


FIG. 6. Changes in mean precipitation, precipitation intensity, precipitation frequency, precipitable water and near-surface specific humidity (first model level $z = 37.5$ m) in the various cases (see Table 1 for a description of the runs). All the quantities shown are changes in time-domain averages and are given in % K⁻¹.

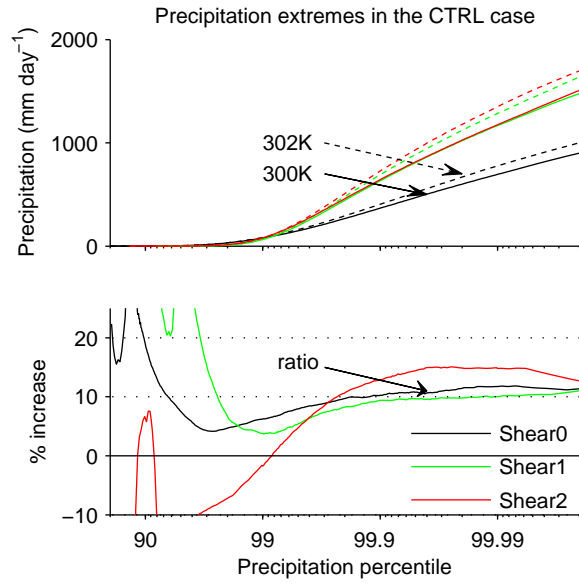


FIG. 7. Changes in the distribution of hourly mean pointwise precipitation accompanying a 2 K SST increase in the control case (CTRL see Table 1 for details) for various shears. The top panel shows the values of precipitation percentiles in mm day^{-1} in the cold and warm simulations. The bottom panel shows the fractional increase in rainfall rates between those two runs.

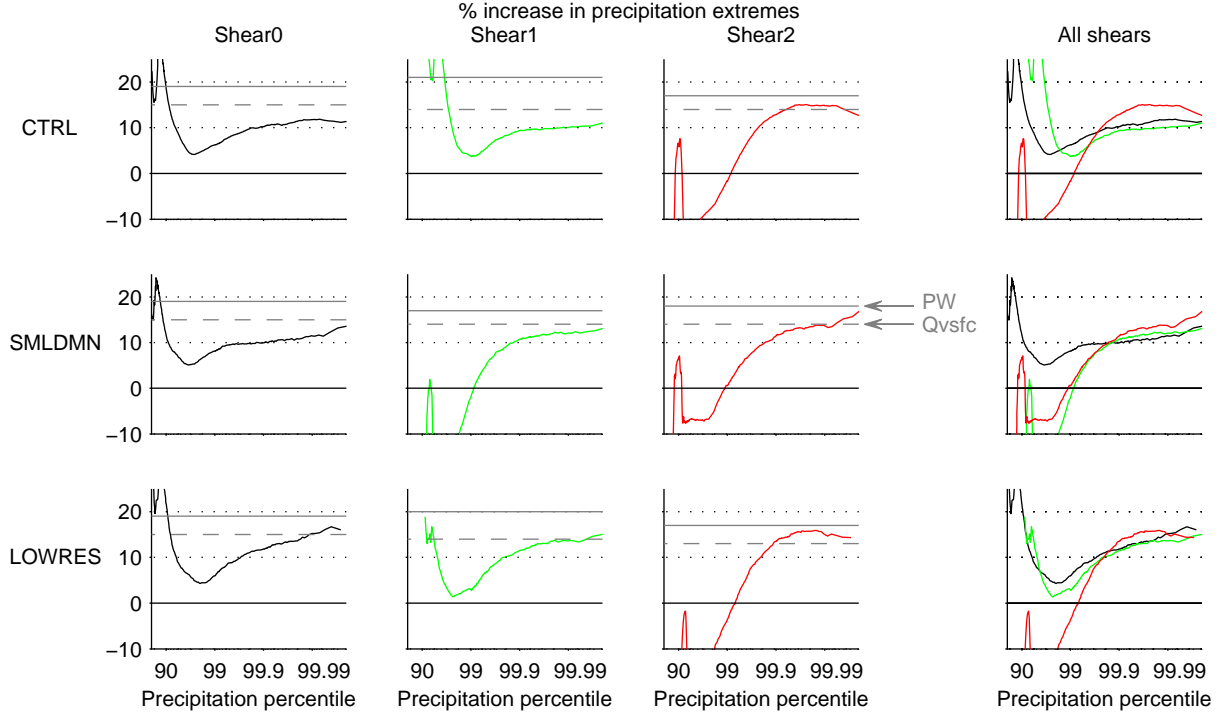


FIG. 8. Changes in the distribution of hourly mean pointwise precipitation accompanying a 2 K SST increase for various cases (CTRL, SMLDMN and LOWRES, see Table 1 for details) and shears. All the values are in %. The changes in precipitable water and near-surface specific humidity are shown as gray solid and dashed lines respectively. To ease comparison, the curves for various shears are superimposed on the right panels.

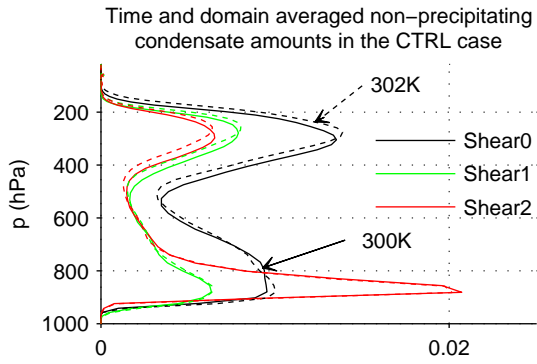


FIG. 9. Vertical profiles of non-precipitating condensate amounts (i.e. clouds, in g kg^{-1}) in the control case, domain and time averaged, for various shears.

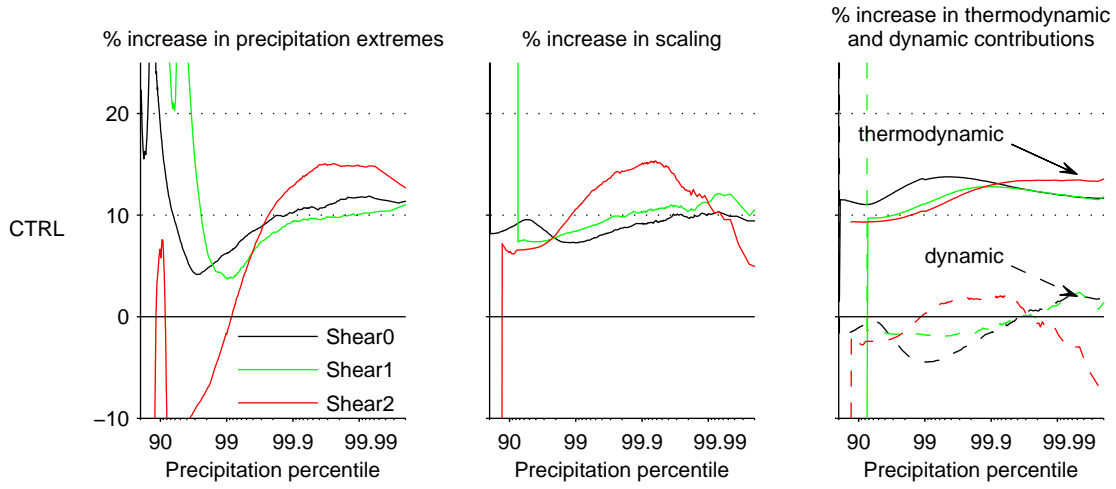


FIG. 10. Changes in precipitation extremes (left panel), in the scaling (3) (middle panel) and in the dynamic and thermodynamic parts of the scaling (right panel) in the CTRL case. All the values are in %.



FIG. 11. Same as Fig. 10, but the middle and right panels show changes in the rough estimate (7) $(\rho w)_{500} < q_v >_{BL}$ (where $< . >$ denotes time and spatial mean). Its thermodynamic part is $\delta < q_v >_{BL}$, and its dynamic part is $\delta(\rho w)_{500}$. All the values are in %.

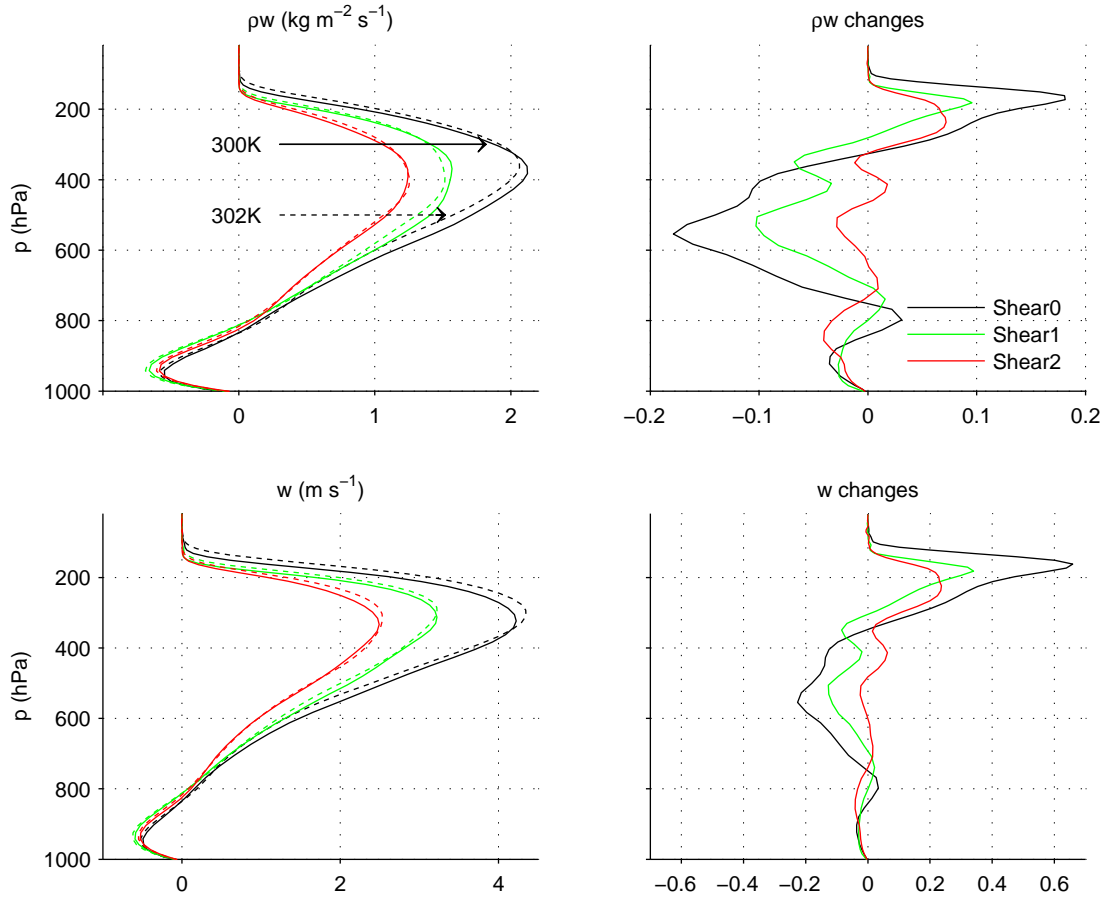


FIG. 12. Vertical mass flux (top panels) and vertical velocities (bottom panels) in the control case at the 99.95th percentile of precipitation for various shears. The values are shown on the left panels, and the changes between the cold and warm runs are shown on the right panels.